A scaling law for the shear-production range of second-order structure functions

Y. Pan and M. Chamecki†

Department of Meteorology, Pennsylvania State University, University Park, PA 16802, USA

(Received ?; revised ?; accepted ?. - To be entered by editorial office)

Dimensional analysis suggests that the dissipation length scale ($\ell_\epsilon = u_\star^3/\epsilon$) is the appropriate scale for the shear-production range of second-order streamwise structure function in neutrally stratified turbulent shear flows near solid boundaries, including smooth- and rough-wall boundary layers and shear layers above canopies (e.g., crops, forests and cities). These flows have two major characteristics in common: (i) a single velocity scale, i.e., the friction velocity ($u_\star$) and, (ii) the presence of large eddies that scale with an external length scale much larger than the local integral length scale. No assumptions are made about the local integral scale, which is shown to be proportional to ℓ_ϵ for the scaling analysis to be consistent with Kolmogorov's result for the inertial subrange. Here ϵ is the rate of dissipation of turbulent kinetic energy (TKE) that represents the rate of energy cascade in the inertial subrange. The scaling yields a log-law dependence of the second-order streamwise structure function on (r/ℓ_ϵ), where r is the streamwise spatial separation. This scaling law is confirmed by large-eddy simulation (LES) results in the roughness sublayer above a model canopy, where the imbalance between local production and dissipation of TKE is much greater than in the inertial layer of wall turbulence and the local integral scale is affected by two external length scales. Parameters estimated for the log-law dependence on (r/ℓ_ϵ) are in reasonable agreement with those reported for the inertial layer of wall turbulence. This leads to two important conclusions. Firstly, the validity of the ℓ_ϵ-scaling is extended to shear flows with much greater imbalance between production and dissipation, indicating possible universality of the shear-production range in flows near solid boundaries. Secondly, from a modeling perspective, ℓ_ϵ is the appropriate scale to characterize turbulence in shear flows with multiple externally imposed length scales.

Key words:

1. Introduction

From the perspective of turbulence theory, the flow over a canopy (e.g., crops, forests and cities) in the neutrally stratified atmospheric boundary layer (ABL) presents an interesting opportunity to study scaling and universality of shear layers with multiple external length scales. Early studies idealized flow over canopies as a superposition of canopy wakes and boundary-layer turbulence over a displaced wall (reviewed by Raupach & Thom 1981). This reasoning and the small scale nature of the wakes of plant elements imply that turbulent motions above the canopy are primarily scaled by the distance from the wall, $(z - d_0)$, known as the inertial layer length scale. The displacement height, d_0, is associated with the mean height of momentum absorption (Thom 1971;

† Email address for correspondence: chamecki@psu.edu

Jackson 1981). However, significant departures from the inertial layer turbulence are clearly seen in measurements within the canopy roughness sublayer, which extends from the ground to approximately three canopy heights (Kaimal & Finnigan 1994). As shown by the important work of Raupach *et al.* (1996), the canopy roughness sublayer is more analogous to a mixing layer than to a rough-wall boundary layer due to its inflectional mean velocity profile and consequent flow instabilities. Second- and third-order turbulence statistics and the significant imbalance between production and dissipation of the turbulent kinetic energy (TKE) observed in shear layers above canopies are also similar to those in mixing layer flows. The canopy-mixing layer analogy identifies a shear length scale (ℓ_s), defined as the mean velocity divided by the mean velocity shear at canopy top, to be the predominant length scale within the canopy roughness sublayer (Raupach *et al.* 1996). Thereafter, the flow above vegetation canopies is typically viewed and modeled as the superposition of mixing layer and boundary layer eddies over a displaced rough wall (e.g., Poggi *et al.* 2004). In summary, the flow above a canopy represents a combination of two well studied canonical shear flows (rough-wall boundary layer and mixing layer), with two distinct external length scales (the inertial length scale ($z - d_0$) and the mixing layer scale (ℓ_s)) and a large imbalance between local production and dissipation of TKE.

The energy density within the production range is of particular interest. For neutrally stratified flows, the shear layer above the canopy and the inertial layer in the wall turbulence have two characteristics in common: (i) a single velocity scale, i.e., the friction velocity ($u_\star$) and, (ii) the presence of large eddies that scale with an external length scale much larger than the local integral length scale. These two characteristics are the major conditions used by Perry *et al.* (1986) to conduct dimensional analysis for wall-bounded flows, showing that a k^{-1} scaling was expected in the production range for the spectral energy density on scales greater than the local integral scale (k is the wavenumber). However, experimental evidence of the k^{-1} spectrum in wall-bounded flows is elusive, mainly due to the aliasing problem associated with one-dimensional spectrum in flows with finite Reynolds number (Tennekes & Lumley 1972; Davidson 2004). The second-order streamwise spatial structure function, $\langle \Delta u^2(r) \rangle$, is an analogous counterpart to the spectrum of streamwise velocity. Physically $\langle \Delta u^2(r) \rangle$ can be considered (roughly) as the cumulative energy of eddies of size r and less, and $d\langle \Delta u^2(r) \rangle / dr$ can be considered as the energy density (Davidson 2004). Here $\langle\rangle$ indicates an ensemble average, u is the streamwise velocity, and r is the streamwise spatial separation. Davidson *et al.* (2006) showed clear experimental evidence of a logarithmic region in $\langle \Delta u^2(r) \rangle$ in wall-bounded flows, where the k^{-1} spectrum was unclear. The authors concluded that, compared with the one-dimensional spectrum, the structure functions provide a clearer diagnostic for analyzing the scaling of turbulent motions. Recent theoretical and experimental results of second- and higher-order structure functions within the inertial layer of moderate-Reynolds-number wall turbulence (Davidson & Krogstad 2014) show that the length $\ell_\epsilon = u_\star^3/\epsilon$ is a more appropriate scale than the inertial layer length scale. The dissipation rate, ϵ, represents the energy cascade in the inertial subrange. Hereafter we follow Townsend (1958) and refer to ℓ_ϵ as the dissipation length scale. Note that ℓ_ϵ is on the same order of the integral scales, and is different from the viscous dissipation (Kolmogorov) length scale. The theory proposed by Davidson & Krogstad (2014) postulated that integral-scale eddies scaled with r, $u_\star$, and ϵ, leaving out the integral length scale (ℓ). However, the absence of ℓ as a relevant length scale in the dimensional analysis is hard to justify *a-priori*, as it implies universality of integral-scale eddies.

The objective of this work is to investigate the validity of the logarithmic ℓ_ϵ-scaling in the roughness sublayer above the canopy, which is characterized by two external length scales and exhibits much greater imbalance between production and dissipation of TKE

than the inertial layer of wall turbulence. Dimensional analysis in §2 suggests a logarithmic dependence of the production range $\langle \Delta u^2(r) \rangle$ on (r/ℓ_ϵ) is expected for shear flows near solid boundaries, with no specific assumptions about the local integral scales or the production and dissipation of turbulent kinetic energy (TKE). By following Perry *et al.* (1986) and explicitly including the integral length scale in the analysis, we avoid postulating the existence of universal scaling as done by Davidson & Krogstad (2014). However, differently from Perry *et al.* (1986), a local balance between production and dissipation of TKE is not invoked in the obtention of the inertial subrange. Instead, by requiring the analysis to be consistent with Kolmogorov's scaling in the inertial subrange, we obtain $\ell \propto \ell_\epsilon$, formally justifying the ℓ_ϵ-scaling. Large-eddy simulation (LES) results validated against field experimental data (described in §3) are used to identify the logarithmic ℓ_ϵ-scaling in the roughness sublayer above the canopy (§4). Simulation results show a convincing collapse of $\langle \Delta u^2(r) \rangle$ when r is normalized by ℓ_ϵ (see §4.3). Conclusions follow in § 5.

2. The scaling law for the second-order streamwise structure function

For turbulent motions within the inertial layer of wall-bounded flows, Perry *et al.* (1986) proposed three ranges of spatial scales with distinct scalings for the energy distribution: (1) a universal range in which motions are uniquely determined by the kinematic viscosity (ν) and the rate of dissipation of TKE (ϵ), (2) a shear-production range in which motions are scaled by the integral length scale (ℓ) and the friction velocity ($u_\star$), and (3) an inactive range in which motions are scaled by the boundary layer thickness (δ) and the friction velocity ($u_\star$). Perry *et al.* (1986) specified $\ell \propto z$ because they were only interested in the inertial layer of wall turbulence. Because this assumption is inapplicable to the canopy roughness sublayer (Raupach *et al.* 1996), we retain the use of ℓ. Perry *et al.* (1986) conducted a dimensional analysis for the streamwise velocity spectrum, matching the spectral energy density for the overlap of adjacent ranges. Here we apply the same dimensional analysis approach to the second-order streamwise spatial structure function,

$$\langle \Delta u^2(r) \rangle = \langle [u(\boldsymbol{x} + r\hat{\boldsymbol{e}}_x, t) - u(\boldsymbol{x}, t)]^2 \rangle, \tag{2.1}$$

where $\boldsymbol{x}$ is the position vector, r is the spatial separation, $\hat{\boldsymbol{e}}_x$ is the unit vector in the streamwise direction, and t is the time. We write

$$\langle \Delta u^2 \rangle = f_1(\nu, \epsilon, r), \quad \langle \Delta u^2 \rangle = f_2(\ell, u_\star, r), \quad \langle \Delta u^2 \rangle = f_3(\delta, u_\star, r), \tag{2.2}$$

for the universal, shear-production and inactive ranges, respectively. The matching of energy density (given by $d\langle \Delta u^2(r) \rangle / dr$) is performed for the overlap of adjacent ranges.

The matching of $d\langle \Delta u^2(r) \rangle / dr$ for the overlap of the shear-production and inactive ranges is equivalent to the approach taken by Davidson & Krogstad (2014), except that Davidson & Krogstad (2014) used ϵ instead of ℓ in the scaling of integral-scale eddies (f_2). In order to avoid postulating universality of the production range, we retain the use of ℓ and rewrite the matching procedure following the steps from Perry *et al.* (1986). For the shear-production range, we have

$$\left[d\langle \Delta u^2(r) \rangle / dr \right] / (u_\star^2 / \ell) = F_2(r/\ell). \tag{2.3}$$

For the inactive range, we have

$$\left[d\langle \Delta u^2(r) \rangle / dr \right] / (u_\star^2 / \delta) = F_3(r/\delta). \tag{2.4}$$

In the overlap of these two ranges, (2.3) and (2.4) are both valid, and therefore

$$F_2(r/\ell) / F_3(r/\delta) = \ell/\delta = (r/\delta)/(r/\ell), \tag{2.5}$$

suggesting that $F_2(r/\ell) \propto (r/\ell)^{-1}$. Thus, we rewrite (2.3) as

$$\left[d\langle\Delta u^2(r)\rangle/d(r/\ell)\right]/u_\star^2 = B_2/(r/\ell), \tag{2.6}$$

where B_2 is a universal constant. Integrating (2.6) yields,

$$\langle\Delta u^2(r)\rangle/u_\star^2 = A_2' + B_2\ln(r/\ell), \tag{2.7}$$

where A_2' is a constant of integration.

This log-law expression for the second-order structure function was also obtained by Davidson *et al.* (2006) by postulating that $r\left[d\langle\Delta u^2(r)\rangle/dr\right]$ is a constant proportional to $u_\star^2$ within the overlap of shear-production and inactive ranges. Physically $r\left[d\langle\Delta u^2(r)\rangle/dr\right]$ is a measure of the energy contained by eddies of size r on a $\ln(r)$ scale. Davidson *et al.* (2006) specified $\ell \propto z$ for the inertial layer of wall turbulence. The prediction $\langle\Delta u^2(r)\rangle \propto \ln(r/z)$ has been confirmed by laboratory and field experimental data (Davidson *et al.* 2006; Davidson & Krogstad 2009; de Silva *et al.* 2015). More recently, Davidson & Krogstad (2014) noted that $\ell \propto \ell_\epsilon$ collapses experimental data better than $\ell \propto z$. The authors also suggest that ℓ_ϵ is a more general length scale, valid for other shear flows. de Silva *et al.* (2015) argued that for high-Reynolds-number wall-bounded flows, local production and dissipation of TKE within the inertial layer are in approximate balance ($\mathcal{P}/\epsilon \approx 1$) and $\ell_\epsilon \approx \kappa z$, where $\kappa = 0.4$ is the von Kármán constant. However, for imbalanced local production and dissipation of TKE within the inertial layer of moderate-Reynolds number wall turbulence ($1 < \mathcal{P}/\epsilon < 1.4$), experimental data favor the use of ℓ_ϵ in place of z to scale the second-order structure function (Davidson & Krogstad 2014).

We now formally justify $\ell \propto \ell_\epsilon$ as a requirement for $F_2(r/\ell)$ in the overlap between the shear-production and universal range to be consistent with Kolmogorov's scaling in the inertial subrange (Kolmogorov 1941)

$$\langle\Delta u^2(r)\rangle = C_2(r\epsilon)^{2/3}, \tag{2.8}$$

where C_2 is a universal constant. Note that the $-5/3$ spectral counterpart of this scaling, has been convincingly observed in the roughness sublayer above corn and forest canopies (Shaw *et al.* 1974; Wilson *et al.* 1982; Kaimal & Finnigan 1994; van Hout *et al.* 2007). Plugging (2.8) into (2.3) yields

$$F_2(r/\ell) = (2/3)C_2(\ell/\ell_\epsilon)^{2/3}(r/\ell)^{-1/3}. \tag{2.9}$$

Because $F_2(r/\ell)$ is only a function of (r/ℓ), ℓ/ℓ_ϵ must be a constant, implying $\ell \propto \ell_\epsilon$. This conclusion is consistent with the statement from Townsend (1958) that ℓ and ℓ_ϵ are approximately equal in constant density flows. Therefore (2.7) becomes

$$\langle\Delta u^2(r)\rangle/u_\star^2 = A_2 + B_2\ln(r/\ell_\epsilon), \tag{2.10}$$

where A_2 is a constant of integration. Equation (2.10) is expected to hold for the overlap of the shear-production and inactive ranges regardless of the specific details of the local integral scale or the production and dissipation of TKE.

3. Description of field experimental data and large-eddy simulations

3.1. *Description and analysis of experimental data*

The experimental data were obtained using sonic anemometers deployed at five heights in a large maize field $z/h = 1/3$, $2/3$, 1, $4/3$ and $5/3$ (Gleicher *et al.* 2014). Velocity time series were sampled at a frequency of 20 Hz and statistics were computed using a 7.5-hour period of approximately stationary turbulence, when $u_\star = 0.51$ m s^{-1}. This period

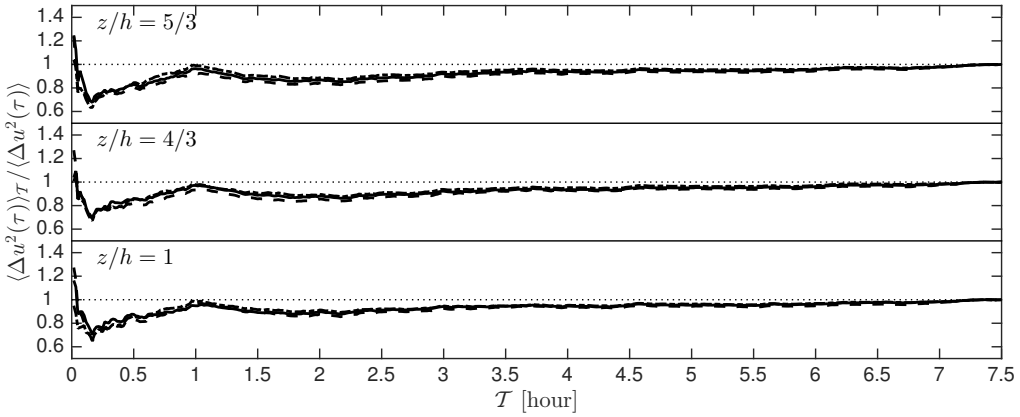

FIGURE 1. The second-order streamwise temporal structure function ($\langle \Delta u(\tau) \rangle$) evaluated using an averaging time interval $\mathcal{T}$ normalized by the values calculated using the entire 7.5-hour period of approximately stationary turbulence (no *subscript*). Results shown for time lags $\tau/(\ell_\epsilon/\langle u \rangle) = 1$, 5 and 10 (represented using *dashed, solid and dash-dotted lines*, respectively) at $z/h = 1$, 4/3 and 5/3.

corresponds to over 25, 000 integral time scales, allowing good sampling of extreme events and motions at spatial scales comparable to the integral length scale (Chamecki 2013). For motions within the inertial subrange, hot-film and particle image velocimetry (PIV) measurements (Shaw *et al.* 1974; Wilson *et al.* 1982; van Hout *et al.* 2007) provide more accurate sampling than sonic anemometers. More specifically, Horst & Oncley (2006) reported non-negligible path averaging errors for sonic anemometer sampling of motions within the inertial subrange.

The scaling proposed in §2 is applied to spatial structure functions, whereas only the temporal structure functions can be obtained from field data measured at fixed locations. The second-order streamwise temporal structure function is defined as

$$\langle \Delta u^2(\tau) \rangle = \langle [u(\boldsymbol{x}, t+\tau) - u(\boldsymbol{x}, t)]^2 \rangle, \tag{3.1}$$

where τ is the time separation. As shown later in §4.2, Taylor's hypothesis of frozen turbulence is inapplicable within the canopy roughness sublayer, and using the temporal structure functions to assess spatial scalings is inaccurate. Both the spatial and temporal structure functions can be obtained from LES results of the resolved velocity. Thus, LES results of spatial structure functions are used to assess the scalings (§4.3), while field data of temporal structure functions are critical for assessing the fidelity of LES results (§4.2).

The convergence of statistics obtained from field data is evaluated by investigating the variability caused by changing the length of the averaging time interval ($\mathcal{T}$) used for analysis (as done by Liu *et al.* 1994). Fig. 1 shows that the second-order structure functions at $z/h = 1$, 4/3 and 5/3 converge within an averaging time interval of 3 hours or less for the range of time lags of interest in the present analysis.

3.2. *LES model setup and analysis of results*

The LES model employed here was described in detail by Pan *et al.* (2014*a*,*b*). The effect of the model vegetation canopy on the flow is represented by a distributed drag that dissipates the kinetic energy of the flow,

$$\boldsymbol{f} = -C_D a |\tilde{\boldsymbol{u}}| \tilde{\boldsymbol{u}}, \tag{3.2}$$

TABLE 1. The number of grid points, grid spacing, and the number of vertical grids occupied by the model canopy used for fine, median and coarse resolution simulations.

Resolution	Number of grid points $N_x \times N_y \times N_z$	Grid spacing $\Delta_x \times \Delta_y \times \Delta_z$	Number of vertical grids occupied by the model canopy
Fine	$560 \times 224 \times 400$	0.375 m $\times$0.375 m $\times$0.13125 m	16
Median	$420 \times 168 \times 300$	0.5 m $\times$0.5 m $\times$0.175 m	12
Coarse	$280 \times 112 \times 200$	0.75 m $\times$0.75 m $\times$0.2625 m	8

where C_D is the drag coefficient, a is the leaf area density, and $\tilde{\boldsymbol{u}}$ is the resolved velocity. The model corn canopy is homogeneous and infinite in both horizontal directions, and the profile of leaf area density is obtained from experimental data (see Gleicher *et al.* 2014, and reference therein). The effect of reconfiguration (i.e., bending and streamlining) of flexible canopy elements is represented using a drag coefficient modeled as a power-law function of velocity capped by an upper limit (Pan *et al.* 2014*b*), $C_D = \min\left((|\tilde{\boldsymbol{u}}|/A)^B, C_{D,\max}\right)$, where $A = 0.22$ m s^{-1}, $B = -2/3$, and $C_{D,\max} = 0.8$. When the velocity is low, the reconfiguration is negligible, and thus $C_D \approx C_{D,\max}$. When the velocity is high, the reconfiguration is strong, and thus $C_D \approx (|\tilde{\boldsymbol{u}}|/A)^B$. The power-law exponent, $B = -2/3$, is the Vogel number reported by theoretical and laboratory studies for simple bending (Alben *et al.* 2002; Gosselin *et al.* 2010).

Three LES runs using different grid resolution were conducted with a friction velocity, $u_\star = \langle u'w' \rangle_h^{1/2} = 0.51$ m s^{-1}, where $u' = u - \langle u \rangle$ and $w' = w - \langle w \rangle$ are the turbulent fluctuations of streamwise and vertical velocity components, and the subscript "h" indicates values at the top of the canopy ($h = 2.1$ m). The simulation domain was a box with $L_x \times L_y \times L_z = 100h \times 40h \times 25h$. The model canopy occupies the entire horizontal domain and the lowest one canopy height of the vertical domain. Table 1 shows the number of grid points, grid spacing, and the number of vertical grids occupied by the model canopy used for fine, median and coarse resolution simulations. An additional median resolution simulation varying the friction velocity by a factor of 5 ($u_\star = 0.1$ m s^{-1}) was conducted to investigate the sensitivity of results to Reynolds number. Supplementary simulations on a smaller domain size ($L_x \times L_y \times L_z = 20h \times 20h \times 10h$) were conducted to determine the range of scales for which the spatial structure functions are not affected by domain size.

The LES runs used the Lagrangian scale-dependent dynamic Smagorinsky subgrid-scale (SGS) model (Bou-Zeid *et al.* 2005). The simulation was driven by a mean pressure gradient force. Viscous, Coriolis and buoyancy effects were not considered. Predictions of turbulence statistics up to the third-order, the strength of quadrant events (e.g., sweeps, ejections and inward and outward interactions), and the fractions of momentum flux transported in different event quadrants agree well with the field experimental data (Pan *et al.* 2014*b*). The median and coarse resolution simulations were conducted using a timestep of $\Delta_t = 0.005$ s, while the fine resolution simulation were conducted using a timestep of $\Delta_t = 0.004$ s. Turbulence statistics were calculated using statistically steady state flow periods of 45 min for the median and coarse resolution simulations and 30 min for the fine resolution simulation. For a given vertical position, statistics were calculated using the instantaneous velocity field within the entire horizontal domain at

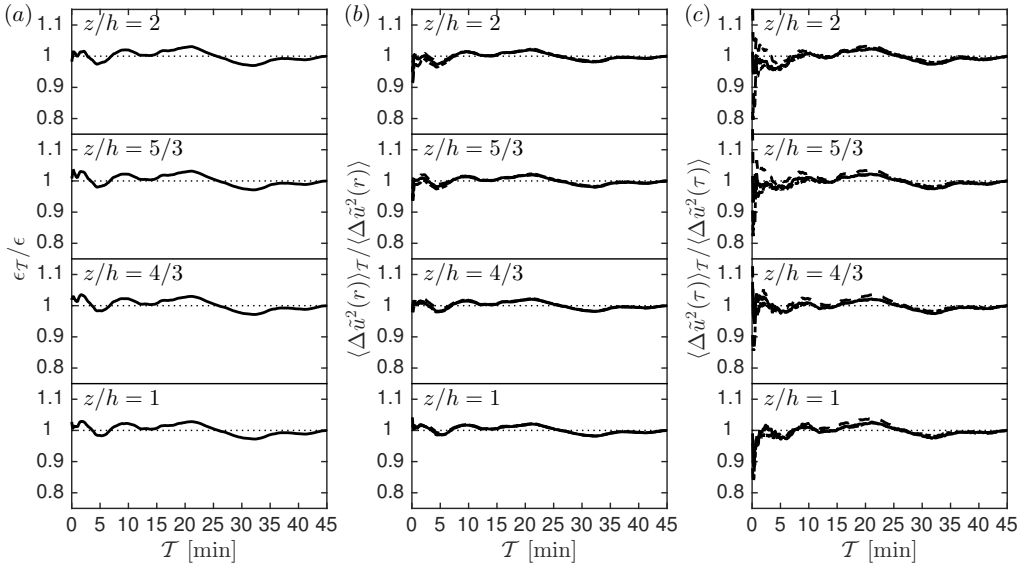

FIGURE 2. The results of the TKE dissipation rate (ϵ), the second-order streamwise spatial structure function ($\langle\Delta\tilde{u}^2(r)\rangle$), and the second-order streamwise temporal structure function ($\langle\Delta\tilde{u}^2(\tau)\rangle$) evaluated using an averaging time interval $\mathcal{T}$ normalized by the values calculated using the entire statistically steady state periods (no *subscript*). Results are obtained from the median resolution simulation with $u_\star = 0.51$ m $^{-1}$ and shown for selected heights, $z/h = 1$, 4/3, 5/3 and 2. The structure functions are shown for selected scales, $r/\ell_\epsilon = 1$, 5 and 10 (b) and $\tau/(\ell_\epsilon/\langle u\rangle) = 1$, 5 and 10 ($c$), represented by *dashed, solid and dash-dotted lines*, respectively.

each timestep and then averaged in time. The spatial structure functions were calculated using snapshots of the instantaneous velocity fields within the entire domain output every 1000 timesteps. For the median and coarse resolution simulations, 540 snapshots were output every 5 s. For the fine resolution simulation, 450 snapshots were output every 4 s. The temporal structure functions were calculated using time series output every timestep at a specified crossflow sectional plane.

In the analysis of simulation results, the displacement height was determined as the mean height of the distributed drag following Thom (1971) and Jackson (1981), yielding $d_0/h = 0.78$. The dissipation rate of TKE was estimated from the SGS dissipation rate (Bou-Zeid *et al.* 2010), which is given by

$$\epsilon = -\langle \boldsymbol{\tau}_{\mathrm{SGS}} : \tilde{\boldsymbol{S}} \rangle, \tag{3.3}$$

where $\boldsymbol{\tau}_{\mathrm{SGS}}$ is the SGS stress tensor and $\tilde{\boldsymbol{S}} = \left(\boldsymbol{\nabla}\tilde{\boldsymbol{u}} + (\boldsymbol{\nabla}\tilde{\boldsymbol{u}})^{\mathrm{T}}\right)/2$ is the filtered strain rate tensor. The scale-dependent SGS model provides reliable estimates of the cascade of TKE from resolved scales to subgrid scales (Bou-Zeid *et al.* 2005). The convergence of LES results is also evaluated by investigating the change in the turbulence statistics with the length of the averaging time interval ($\mathcal{T}$) used for analysis. For the median resolution simulation with $u_\star = 0.51$ m s^{-1}, Fig. 2 shows that results of the TKE dissipation rate and the second-order structure functions at $1 < z/h < 2$ converge within an averaging time interval of 10 min or less. Simulations with alternative grid resolution and friction velocity require a similar averaging time interval for these statistics to converge (not shown). The use of spatial averaging for the analysis of LES results yields shorter averaging periods required for convergence in comparison to those needed for the field data.

4. Results and Discussions

4.1. *Characteristics of the roughness sublayer above the model canopy*

The region of interest here is the shear layer above the model canopy and within the lowest 20% of the domain, corresponding to the region $1 < z/h < 5$. Within this region, simulations with $u_\star = 0.51$ m s^{-1} yield the Reynolds number for the flow, $Re = \ell_\epsilon u_\star/\nu$, ranging from 2.6×10^4 to 1.4×10^5. The roughness Reynolds number, $Re^\star = hu_\star/\nu = 7.2\times10^4$, where $h = 2.1$ m is the canopy height. The Taylor microscale Reynolds number, $Re_\lambda = \lambda u_\star/\nu$, ranges from 1.1×10^3 to 2.8×10^3. For the median resolution simulation, the effective Reynolds number, $Re_{\mathrm{LES}} = (\eta/\eta_{\mathrm{LES}})^{4/3}Re$ (Muschinski 1996), ranges from 34 to 236. The effective roughness Reynolds number, $Re^\star_{\mathrm{LES}} = (\eta/\eta_{\mathrm{LES}})^{4/3}Re^\star = 92$. Here $\nu = 1.48 \times 10^{-5}$ m^2 s^{-1} is the kinematic viscosity of air, $\lambda = \left(15\nu\sigma_u^2/\epsilon\right)^{1/2}$ is the Taylor microscale, $\eta = \left(\nu^3/\epsilon\right)^{1/4}$ is the Kolmogorov length scale, $\eta_{\mathrm{LES}} = c_s\Delta$ is the SGS mixing length, c_s is the Smagorinsky coefficient, and $\Delta = (\Delta_x\Delta_y\Delta_z)^{1/3}$ is the characteristic grid spacing (Scotti *et al.* 1993). The roughness Reynolds number varies with friction velocity, but not with grid resolution. The effective roughness Reynolds number varies with grid resolution, but not with friction velocity. The fine and coarse resolution simulations yield $Re^\star_{\mathrm{LES}} = 136$ and 54, respectively.

Fig. 3(a) shows the vertical profiles of the production and dissipation rates of TKE normalized by $u_\star^3/h$. These dimensionless vertical profiles are independent of grid resolution and friction velocity (not shown). The insensitivity of ϵ estimated using (3.3) to grid spacing implies that the rate of energy cascade provides reasonable estimates of the rate of TKE dissipation. The reliability of LES estimates of $\epsilon/(u_\star^3/h)$ immediately above the model canopy is further supported by the good agreement with dissipation rates estimated from PIV measurements above a mature corn canopy obtained by van Hout *et al.* (2007) (*dashed line* compared with *crosses* in Fig. 3a). Close to the canopy top, the ratio $\mathcal{P}/\epsilon \approx 3$ (Fig. 3b), a value much greater than that observed in the inertial layer of wall turbulence and more characteristic of mixing layers (Rogers & Moser 1994). For $z/h > 2.5$, the production and dissipation of TKE are almost in balance (Fig. 3a, b), and the production length scale ($\ell_\mathcal{P} = u_\star^3/\mathcal{P}$) approaches $\kappa(z - d_0)$ (*solid line* compared with *vertical dotted line* in Fig. 3c). These features indicate the recovery of an inertial layer, and thus $z/h = 2.5$ is determined as the upper boundary of the canopy roughness sublayer.

Within the roughness sublayer above the canopy ($1 < z/h < 2.5$), two external length scales coexist: $(z-d_0)$ associated with inertial layer eddies and $\ell_s = \langle u\rangle_{z=h}/(\partial\langle u\rangle/\partial z)_{z=h}$ associated with mixing layer eddies (Raupach *et al.* 1996). As expected, ℓ_s (*dash-dotted line* in Fig. 3c) is much larger than $\kappa(z - d_0)$ near the canopy top, and it becomes significantly smaller than $\kappa(z - d_0)$ above the canopy roughness sublayer ($z/h > 2.5$). Even though the production length scale (*solid line* in Fig. 3c) increases as the canopy top is approached, it does not reflect the large coherence of mixing layer eddies that scale on ℓ_s. Interestingly, the dissipation length scale ℓ_ϵ (*dashed line* in Fig. 3c) provides a smooth transition from ℓ_s near the canopy top to $\kappa(z-d_0)$ above the canopy roughness sublayer. These LES results suggest that ℓ_ϵ has the potential to characterize the transition from a mixing-layer flow close to the canopy top to a boundary-layer flow above the canopy roughness sublayer. Thus, LES results support the theoretical analysis in §2 that ℓ_ϵ characterizes the shear-production range turbulent motions.

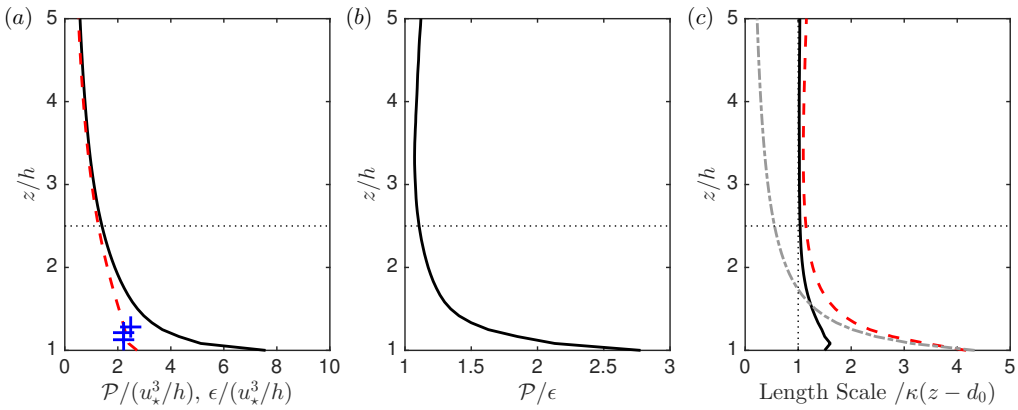

FIGURE 3. LES results of the production ($\mathcal{P}$) and dissipation (ϵ) rates of TKE normalized by $u_\star^3/h$ (a), the ratio $\mathcal{P}/\epsilon$ (b), and the length scales ($\ell_\mathcal{P}$, ℓ_ϵ and ℓ_s) normalized by $\kappa(z-d_0)$ (c) against vertical distance from the ground (z) normalized by canopy height (h). In panel (a), *Solid and dashed lines* indicate $\mathcal{P}/(u_\star^3/h)$ and $\epsilon/(u_\star^3/h)$, respectively. *Crosses* indicate estimates of $\epsilon/(u_\star^3/h)$ from PIV measurements above a corn canopy (van Hout *et al.* 2007). In panel (c), *solid, dashed and dash-dotted lines* indicate $\ell_\mathcal{P}/\kappa(z-d_0)$, $\ell_\epsilon/\kappa(z-d_0)$ and $\ell_s/\kappa(z-d_0)$, respectively. Here $u_\star$ is the friction velocity, d_0 is the displacement height, and $(z-d_0)$, ℓ_s, $\ell_\mathcal{P}$, and ℓ_ϵ are the inertial layer, mixing layer, production, dissipation length scales, respectively. The *horizontal dotted lines* indicate the upper boundary of the canopy roughness layer, $z/h = 2.5$.

4.2. *Evaluation of the second-order streamwise temporal structure function*

We start by using results of temporal and spatial structure functions from the median resolution simulation with $u_\star = 0.51$ m s^{-1} to assess the validity of Taylor's hypothesis of frozen turbulence in the canopy shear layer. Fig. 4a shows that the temporal structure functions converted using Taylor's hypothesis ($\langle\Delta\tilde{u}^2(r=\tau\langle u\rangle)\rangle$) agree well with the spatial structure functions ($\langle\Delta\tilde{u}^2(r)\rangle$) at small scales, but asymptote faster to the maximum value ($2\langle u'^2\rangle$). The cutoff scale for the validity of Taylor's hypothesis increases with increasing distance from the canopy top. Specifically for $z/h > 4/3$ (*blue, cyan, black, green and grey dashed and solid lines* in Fig. 4a), the cutoff scale is greater than $r/l_\epsilon = 3$. The inapplicability of Taylor's hypothesis is expected, given the large values of turbulence intensity ($\sigma_u/\langle u\rangle$) typically observed in canopy shear layers (Fig. 4(b)). Note that spatial structure functions collapse using the ℓ_ϵ-scaling, but their temporal counterparts do not due to inapplicability of Taylor's hypothesis for the production and inactive ranges. Results from simulation using different grid resolutions or friction velocity yield the same conclusion (not shown). The nonequivalence between spatial and temporal structure functions exposes the limitations of field experimental data in assessing structure function scalings (and other related statistics such as correlation functions, integral length scales, etc.) in canopy shear layers.

Fig. 5 shows evaluation of LES results of the second-order temporal structure functions against field experimental data. Note that both hot-film and PIV measurements within the roughness sublayer above corn canopies confirmed the $-5/3$ scaling in the inertial subrange of the spectrum of the streamwise velocity (Shaw *et al.* 1974; Wilson *et al.* 1982; van Hout *et al.* 2007). Within the inertial subrange, Taylor's hypothesis of frozen turbulence is valid (see Fig. 4), and therefore the second-order streamwise temporal structure function ($\langle\Delta u^2(\tau)\rangle$) and the energy density ($d\langle\Delta u^2(\tau)\rangle/d\tau$) are expected to scale as $\tau^{2/3}$ and $\tau^{-1/3}$, respectively. Due to non-negligible path averaging errors associated with sonic anemometer measurements at the frequencies that correspond to the inertial subrange

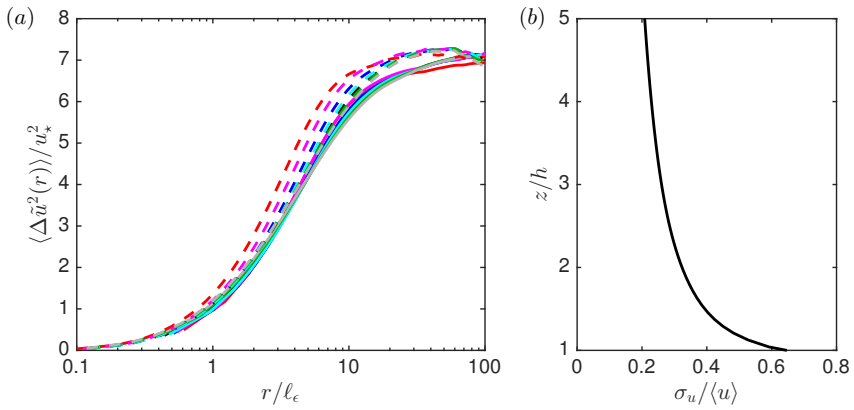

FIGURE 4. (a) LES results of second-order streamwise spatial structure functions ($\langle \Delta\tilde{u}^2(r)\rangle$; *solid lines*) and temporal structure functions converted using Taylor's hypothesis ($\langle \Delta\tilde{u}^2(r=\tau\langle u\rangle)\rangle$; *dashed lines*) normalized by the square of friction velocity ($u_\star^2$) against spatial separation (r) normalized by the dissipation length scale (ℓ_ϵ). *Red, magenta, blue, cyan, black, green and grey lines* indicate results for $1 < z/h < 2$ with an increment of $\Delta z/h = 1/6$. (b) The turbulence intensity ($\sigma_u/\langle u\rangle$) against vertical distance from the ground (z) normalized by canopy height (h), where σ_u and $\langle u\rangle$ are the standard deviation and the mean of the streamwise velocity, respectively.

(Horst & Oncley 2006), the raw field data of $d\langle \Delta u^2(\tau)\rangle/d\tau$ at small scales do not follow $\tau^{-1/3}$ exactly (*black dots* compared with *grey solid lines* in Fig. 5*d–f*). Nevertheless, the $\tau^{-1/3}$ dependence of $d\langle \Delta u^2(\tau)\rangle/d\tau$ in the inertial subrange is approached by raw data from sonic anemometer measurements.

Because LES does not resolve SGS motions, the structure function of the resolved velocity ($\tilde{u}$) is expected to be smaller than the raw field data (*dashed lines* compared with *black dots* in Fig. 5*a–c*). The *vertical dotted lines* in Fig. 5(*d–f*) indicate the cutoff scales for the median resolution simulation, sitting at the transition from the inertial subrange to the overlap of the shear-production and inactive ranges. At subgrid scales, reducing the grid spacing improves the capability of reproducing the energy density (*cyan dashed lines* compared with *red dashed lines* in Fig. 5*d–f* to the left of the *vertical dotted lines*). At resolved scales, the fine and median resolution simulations yield the same energy density, whereas the coarse resolution simulation exhibits a pile-up of energy (*blue dashed lines* compared with *cyan and red dashed lines* in the inset in Fig. 5*f*). In addition, for the fine and median resolution simulations, the scale-dependent dynamic SGS model predicts the same profile of the Smagorinsky coefficient, whereas the coarse resolution simulation results show a reduction of the Smagorinsky coefficient (not shown). Both the pile-up of energy at resolved scales and the reduction of the Smagorinsky coefficient indicate insufficient resolution for the coarse resolution simulation (Bou-Zeid *et al.* 2005). Thus, we conclude that the median grid resolution used here corresponds to the minimum resolution required for the adequate reproduction of turbulence above the maize canopy studied here. For $z/h = 1$, LES results slightly overestimated the energy density of raw experimental data at resolved scales (*dashed lines* compared with *black dots* to the right of the *vertical dotted line* in Fig. 5*d*). For $z/h = 4/3$ and $5/3$, LES results reproduced the energy density of raw experimental data at resolved scales (*dashed lines* compared with *black dots* to the right of the *vertical dotted lines* in Fig. 5*e*, *f*).

To provide a better basis for comparison with LES, a Gaussian filter (Pope 2000) is applied to the experimental data. The filter size, $\Delta_\tau = (4/\sqrt{2})\Delta_x/\langle u\rangle$, is chosen to

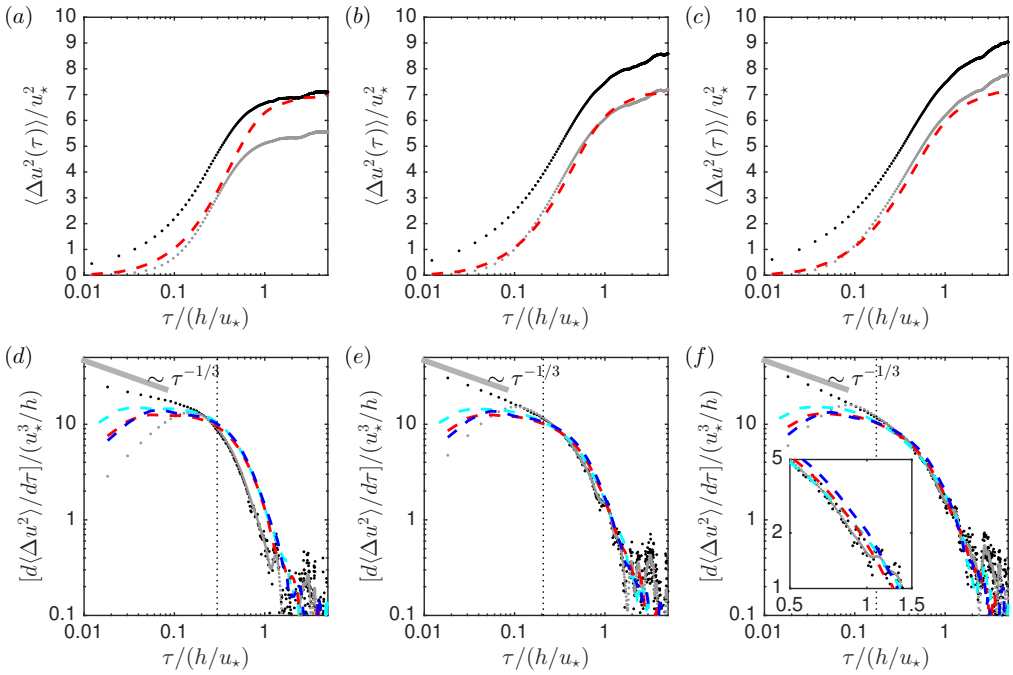

FIGURE 5. Evaluation of LES results of the normalized second-order temporal structure function ($\langle \Delta \tilde{u}^2(\tau) \rangle / u_\star^2$; *a–c*) and the energy density ($\left[d\langle \Delta u^2(\tau) \rangle / d\tau\right] / (u_\star^3/h)$; *d–f*) against field experimental data for $z/h = 1$ (*a*, *d*), 4/3 (*b*, *e*) and 5/3 (*c*, *f*). *Blue, red and cyan dashed lines* indicate LES results from coarse, median and fine resolution simulations, while *black and grey dots* indicate the structure function of raw and filtered experimental velocity data. The *vertical dotted lines* in (*d–f*) indicate the cutoff scales for the median resolution simulation, $\tau = 4\Delta_x/\langle u \rangle$, where $\Delta_x = 0.5$ m. The filter size applied to experimental velocity data, $\Delta_\tau = (4/\sqrt{2})\Delta_x/\langle u \rangle$, are 0.87, 0.61 and 0.51 s for $z/h = 1$, 4/3 and 5/3, respectively.

maintain turbulent motions at spatial scales greater than $4\Delta_x$ (i.e. the scales resolved in the LES). LES results reproduced the second-order streamwise temporal structure function of filtered experimental velocity data for $z/h = 4/3$ and 5/3 (*red dashed lines* compared with *grey dots* in Fig. 5*b*, *c*). Close to the canopy top, the removal of energy from large scales is enhanced by wake production behind individual canopy elements, a feature not represented in the LES model. As expected, for $z/h = 1$, LES results overestimated the structure function of filtered experimental velocity data, especially at large scales $\tau/(h/u_\star) > 0.5$ (*red dashed line* compared with *grey dots* in Fig. 5*a*). Results presented in Fig. 5 suggest that the fine and median resolution simulations are capable of reproducing details of second-order structure functions above the canopy for scales larger than those in the inertial subrange (a finer grid resolution would be needed for inertial subrange scales to be reliable). The analysis presented next focuses on the overlap of shear-production and inactive ranges, where motions are well resolved in the simulations.

4.3. *Scaling of the second-order streamwise spatial structure function*

Fig. 6(*a-c*) shows results of the second-order streamwise spatial structure function of resolved velocity ($\langle \Delta \tilde{u}^2(r) \rangle$) from the median resolution simulation with $u_\star = 0.51$ m s^{-1} against the eddy size (r) normalized by three different length scales ($\kappa(z - d_0)$, $\ell_\mathcal{P}$ and ℓ_ϵ). Within the roughness sublayer layer above the canopy ($1 < z/h < 2.5$), the inertial

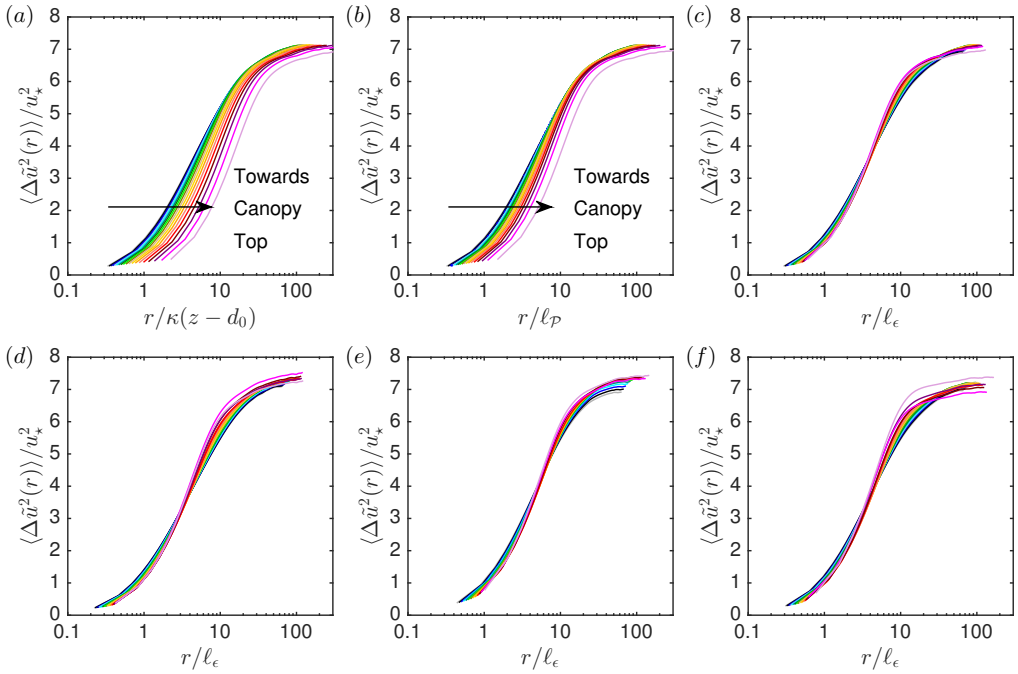

FIGURE 6. LES results of the normalized second-order streamwise spatial structure function of $(\langle \Delta\tilde{u}^2(r)\rangle/u_\star^2)$ against streamwise spatial separation (r) normalized by $\kappa(z-d_0)$ (a), $\ell_\mathcal{P}$ (b) and ℓ_ϵ $(c$–$f)$. Here $(z-d_0)$, $\ell_\mathcal{P}$ and ℓ_ϵ are the inertial layer, production and dissipation length scales. *Solid lines of different colours* indicate results at different heights within the shear layer above the canopy $(1 < z/h < 2.5)$, with an increment of $\Delta z/h = 1/8$, $1/12$ and $1/16$ for coarse (e), median $(a$–$c,\ f)$ and fine (d) resolution simulations. Arrows indicate decreasing vertical coordinate towards the canopy top. Simulations were conducted with $u_\star = 0.51$ m s^{-1} $(a$–$e)$ and 0.1 m s^{-1} (f).

layer, production and dissipation length scales ($(z-d_0)$, $\ell_\mathcal{P}$ and ℓ_ϵ) are not proportional to each other (Fig. 3*b*). LES runs with varying domain sizes (not shown) suggest that the current domain provides reliable estimates of $\langle \Delta\tilde{u}^2(r)\rangle$ for $r/\ell_\epsilon < 20$. Curves representing $\langle \Delta\tilde{u}^2(r)\rangle/u_\star^2$ at different heights do not collapse when r is normalized by $\kappa(z-d_0)$ (Fig. 6*a*) or $\ell_\mathcal{P}$ (Fig. 6*b*), but do collapse when r is normalized by ℓ_ϵ (Fig. 6*c*). The collapse against ℓ_ϵ is robust to changes in grid resolution and friction velocity (Fig. 6*d*–*f*). These results indicate that ℓ_ϵ rather than $(z-d_0)$ or $\ell_\mathcal{P}$ is the correct scaling for the second-order structure function within the shear layer above the canopy.

The overlap of the shear-production and inactive ranges corresponds to spatial scales greater than the integral length scale ($r > \ell \propto \ell_\epsilon$) and much smaller than the boundary layer thickness ($r \ll \delta \sim L_z$). In addition, results in §4.2 suggest that LES resolves spatial scales greater than $4\Delta_x$. Thus we estimate that the resolved overlap of the shear-production and inactive ranges for the present simulation consists of spatial scales $\max(\ell_\epsilon, 4\Delta_x) < r < 0.2L_z$. This range of spatial scales roughly corresponds to $1 < r/\ell_\epsilon < 10$, where a $\ln(r/\ell_\epsilon)$ law is observed for LES results of the second-order structure function (Fig. 6*c*–*f*). Fig. 7 shows the ranges of parameters A_2 and B_2 in (2.10) estimated for each simulation by applying a least square fitting to the logarithmic region ($\max(\ell_\epsilon, 4\Delta_x) < r < 0.2L_z$) of individual curves in Fig. 6(c–f). An additional set of parameters A_2 and B_2 is estimated for each simulation by applying a least square fitting to all the heights together (*circles* in Fig. 7). The ranges of A_2 and B_2 estimated for

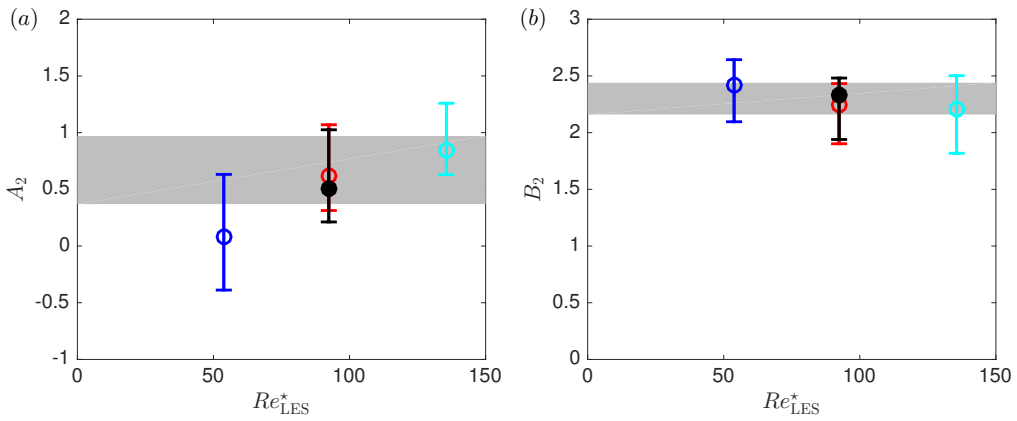

FIGURE 7. Ranges of parameters A_2 (a) and B_2 (b) in (2.10) estimated for each simulation by applying a least square fitting to the logarithmic region $(\max(\ell_\epsilon, 4\Delta_x) < r < 0.2L_z)$ of individual curves in Fig. 6$(c$–$f)$ against the effective roughness Reynolds number $(Re^\star_{\mathrm{LES}})$. *Blue, red and cyan error bars* indicate the ranges estimated for coarse, median and fine resolution simulation with $u_\star = 0.51$ m s^{-1}, while the *black error bar* indicates the ranges estimated for median resolution simulation with $u_\star = 0.1$ m s^{-1}. *Circles that are the same colour as error bars* indicate an additional set of parameters A_2 and B_2 estimated for each simulation by applying a least square fitting to the logarithmic region of all curves in Fig. 6$(c$–$f)$. *Open and filled cirlces* represent simulations with $u_\star = 0.51$ and 0.1 m s^{-1}, respectively. *Grey areas* in (a) and (b) indicate the ranges $0.37 < A_2 < 0.97$ and $2.16 < B_2 < 2.44$ estimated by de Silva *et al.* (2015) using laboratory and field experimental data obtained in the inertial layer of wall turbulence.

fine and median resolution simulations (*cyan, red and black error bars* in Fig. 7) are in reasonable agreement with those estimated by de Silva *et al.* (2015) using laboratory and field experimental data obtained in the inertial layer of wall turbulence ($0.37 < A_2 < 0.97$ and $2.16 < B_2 < 2.44$, represented by *grey areas* in Fig. 7). Varying $u_\star$ by a factor of 5 can change the displacement height by 10% (Pan *et al.* 2016), but it induces negligible changes in the estimated ranges for A_2 and B_2 (*black error bar* compared with *red error bar* in Fig. 7). Fig. 6$(c$–$f)$ confirms the validity of the dimensional analysis presented in §2 in the shear layer above a canopy, while Fig. 7 suggests the possibility of the existence of a fairly universal set of parameters A_2 and B_2 that may hold for a wide range of shear flows.

5. Conclusions

Dimensional analysis following Perry *et al.* (1986) and Davidson & Krogstad (2014) constrained by the scaling within the inertial subrange yields a general prediction for the second-order structure function ($\langle \Delta u^2(r) \rangle$) in the production range of shear flows. The dimensional analysis presented here justifies the assumption of universality of the production range invoked by Davidson & Krogstad (2014) for flows characterized by a single velocity scale in which three distinct ranges of eddy sizes exist, as described by (2.2). The universal and shear-production ranges are common for all shear flows. The eddies with sizes much larger than the local integral scale are less universal, but may not be confined to flows near solid boundaries. Under these conditions, the logarithmic dependence of $\langle \Delta u^2(r) \rangle$ on (r/ℓ_ϵ) is expected to hold. The proportionality between the integral and the dissipation length scales ($\ell \propto \ell_\epsilon$) is a requirement for the dimensional analysis to be consistent with the theory of Kolmogorov (1941). The ℓ_ϵ-scaling and the log-law behaviour at integral scales ($r/\ell_\epsilon > 1$) are confirmed by LES results for the

roughness sublayer above a model corn canopy (a shear layer with two externally imposed length scales and a large imbalance between production and dissipation rates of TKE). The good agreement between parameters in the log-law obtained here and those reported by de Silva *et al.* (2015) for the inertial layer in wall turbulence implies that the key differences between these two types of flows are likely contained in ℓ_ϵ, suggesting possible universality of the shear-production range across different shear flows. In the specific case of a model vegetation canopy studied here, the dissipation length scale exhibits a smooth transition from the shear length scale at the canopy top to the inertial layer length scale at the upper boundary of the canopy roughness sublayer. This result suggests that, from a modeling perspective, ℓ_ϵ is the appropriate scale to characterize turbulent shear flows with multiple imposed length scales.

Acknowledgements This research is supported by the National Science Foundation (NSF) grant AGS1005363.

REFERENCES

Alben, S., Shelley, M. & Zhang, J. 2002 Drag reduction through self-similar bending of a flexible body. *Nature* **420**, 479–481.

Bou-Zeid, E., Higgins, C., Huwald, H., Meneveau, C. & Parlange, M. B. 2010 Field study of the dynamics and modelling of subgrid-scale turbulence in a stable atmospheric surface layer over a glacier. *J. Fluid Mech.* **665**, 480–515.

Bou-Zeid, E., Meneveau, C. & Parlange, M. B. 2005 A scale-dependent Lagrangian dynamic model for large eddy simulation of complex turbulent flows. *Phys. Fluids* **17**, 025105, doi:10.1063/1.1839152.

Chamecki, M. 2013 Persistence of velocity fluctuations in non-Gaussian turbulence within and above plant canopies. *Phys. Fluids* **25**, 1–14.

Davidson, P. A. 2004 *Turbulence: an introduction for scientists and engineers*. Oxford, UK: Oxford University Press, 657 pp.

Davidson, P. A. & Krogstad, P.-Å. 2009 A simple model for the streamwise fluctuations in the log-law region of a boundary layer. *Phys. Fluids* **21**, 055105.

Davidson, P. A. & Krogstad, P.-Å. 2014 A universal scaling for low-order structure functions in the log-law region of smooth-and rough-wall boundary layers. *J. Fluid Mech.* **752**, 140–156.

Davidson, P. A., Nickels, T. B. & Krogstad, P.-Å. 2006 The logarithmic structure function law in wall-layer turbulence. *J. Fluid Mech.* **550**, 51–60.

Gleicher, S. C., Chamecki, M., Isard, S. A., Pan, Y. & Katul, G. G. 2014 Interpreting three-dimensional spore concentration measurements and escape fraction in a crop canopy using a coupled Eulerian-Lagrangian Stochastic model. *Agric. For. Meteorol.* **194**, 118–131.

Gosselin, F., de Langre, E. & Machado-Almeida, B.A. 2010 Drag reduction of flexible plates by reconfiguration. *J. Fluid Mech.* **650**, 319–341.

Horst, T. W. & Oncley, S. P. 2006 Corrections to inertial-range power spectra measured by CSAT3 and Solent sonic anemometers, 1. Path-averaging errors. *Boundary-layer meteorology* **119**, 375–395.

van Hout, R., Zhu, W., Luznik, L., Katz, J., Kleissl, J. & Parlange, M. B. 2007 PIV measurements in the atmospheric boundary layer within and above a mature corn canopy. Part I: Statistics and energy flux. *J. Atmos. Sci.* **64**, 2805–2824.

Jackson, P. S. 1981 On the displacement height in the logarithmic velocity profile. *J. Fluid Mech.* **111**, 15–25.

Kaimal, J. C. & Finnigan, J. J. 1994 *Atmospheric Boundary Layer Flows: Their Structure and Measurement*. New York: Oxford University Press, 289 pp.

Kolmogorov, A. N. 1941 The local structure of turbulence in incompressible viscous fluid for very large Reynolds numbers. In *Dokl. Akad. Nauk SSSR*, , vol. 30, pp. 299–303.

Liu, S., Meneveau, C. & Katz, J. 1994 On the properties of similarity subgrid-scale models as deduced from measurements in a turbulent jet. *J. Fluid Mech.* **275**, 83–119.

Muschinski, A. 1996 A similarity theory of locally homogeneous and isotropic turbulence generated by a Smagorinsky-type LES. *J. Fluid Mech.* **325**, 239–260.

Pan, Y., Chamecki, M. & Isard, S. A. 2014*a* Large-eddy simulation of turbulence and paticle dispersion inside the canopy roughness sublayer. *J. Fluid Mech.* **753**, 499–534.

Pan, Y., Chamecki, M. & Nepf, H. M. 2016 Estimating the instantaneous drag-wind relationship for a horizontally homogeneous canopy. *Boundary-Layer Meteorol.* pp. 1–20, doi:10.1007/s10546-016-0137x.

Pan, Y., Follett, E., Chamecki, M. & Nepf, H. 2014*b* Strong and weak, unsteady reconfiguration and its impact on turbulence structure within plant canopies. *Phys. Fluids* **26**, 105102.

Perry, A. E., Henbest, S. & Chong, M. S. 1986 A theoretical and experimental study of wall turbulence. *J. Fluid Mech.* **165**, 163–199.

Poggi, D., Porporato, A., Ridolfi, L., Albertson, J. D. & Katul, G. G. 2004 The effect of vegetation density on canopy sub-layer turbulence. *Boundary-Layer Meteorol.* **111**, 565–587.

Pope, S. B. 2000 *Turbulent flows*. New Delhi, India: Cambridge Univ. Press, 771 pp.

Raupach, M. R., Finnigan, J. J. & Brunet, Y. 1996 Coherent eddies and turbulence in vegetation canopies: the mixing-layer analogy. *Boundary-Layer Meteorol.* **78**, 351–382.

Raupach, M. R. & Thom, A. S. 1981 Turbulence in and above plant canopies. *Ann. Rev. Fluid Mech.* **13**, 97–129.

Rogers, M. M. & Moser, R. D. 1994 Direct simulation of a self-similar turbulent mixing layer. *Phys. Fluids* **6**, 903–923.

Scotti, A., Meneveau, C. & Lilly, D. K. 1993 Generalized smagorinsky model for anisotropic grids. *Phys. Fluids* **5**, 2306–2308.

Shaw, R. H., Silversides, R. H. & Thurtell, G. W. 1974 Some observations of turbulence and turbulent transport within and above plant canopies. *Boundary-Layer Meteorol.* **5**, 429–449.

de Silva, C. M., Marusic, I., Woodcock, J. D. & Meneveau, C. 2015 Scaling of second- and higher-order structure functions in turbulent boundary layers. *J. Fluid Mech.* **769**, 654–686.

Tennekes, H. & Lumley, J.L. 1972 *A first course in turbulence*. Cambridge, Massachusetts: The MIT Press, 300 pp.

Thom, A. S. 1971 Momentum absorption by vegetation. *Q. J. Roy. Meteorol. Soc.* **97**, 414–428.

Townsend, A. A. 1958 Turbulent flow in a stably stratified atmosphere. *J. Fluid Mech.* **3**, 361–372.

Wilson, J. D., Ward, D. P., Thurtell, G. W. & Kidd, G. E. 1982 Statistics of atmospheric turbulence within and above a corn canopy. *Boundary-Layer Meteorol.* **24**, 495–519.